NACA

RESEARCH MEMORANDUM

TRANSONIC-WIND-TUNNEL INVESTIGATION OF THE EFFECTS OF

LIP BLUNTNESS AND SHAPE ON THE DRAG AND PRESSURE

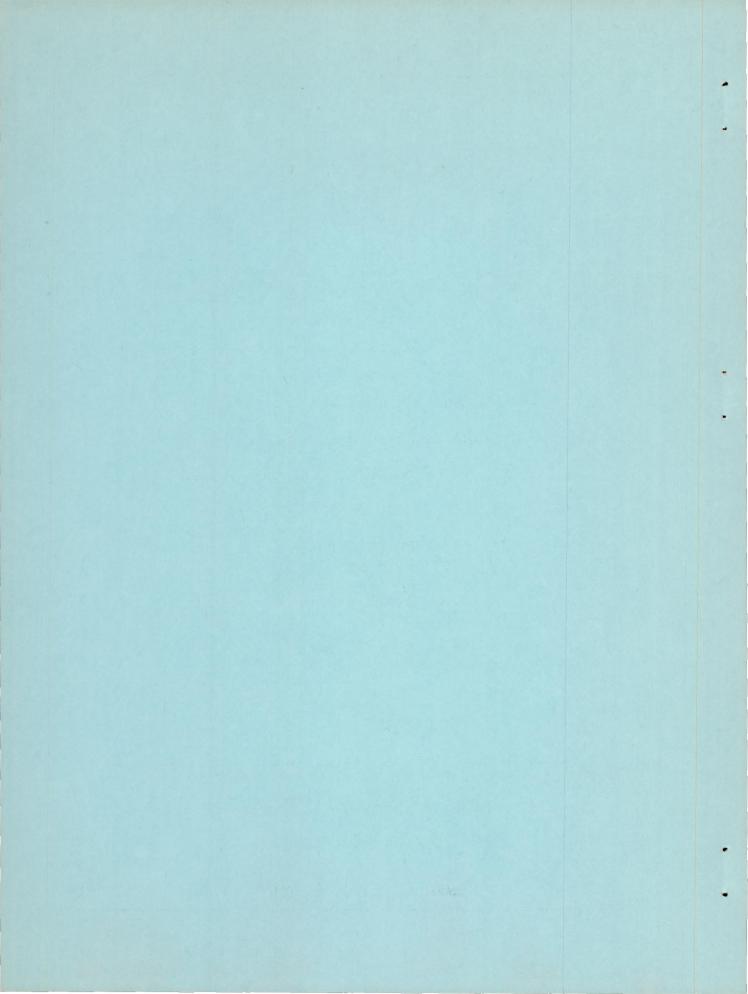RECOVERY OF A NORMAL-SHOCK NOSE INLET

IN A BODY OF REVOLUTION

By Walter B. Olstad

Langley Aeronautical Laboratory
Langley Field, Va.

NATIONAL ADVISORY COMMITTEE
FOR AERONAUTICS
WASHINGTON

NATIONAL ADVISORY COMMITTEE FOR AERONAUTICS

———————

RESEARCH MEMORANDUM

———————

TRANSONIC-WIND-TUNNEL INVESTIGATION OF THE EFFECTS OF

LIP BLUNTNESS AND SHAPE ON THE DRAG AND PRESSURE

RECOVERY OF A NORMAL-SHOCK NOSE INLET

IN A BODY OF REVOLUTION

By Walter B. Olstad

SUMMARY

An investigation has been made to determine the effects of lip bluntness, camber, and leading-edge roundness on the drag and pressure recovery of a normal-shock nose inlet in a body of revolution. Surface pressure distributions over the inlet lip and forebody were also obtained. Configurations with 5° and 10° half-angle conical forebodies were tested. The results were obtained in the Langley 8-foot transonic tunnel at test Mach numbers from 0.4 to 1.14, angles of attack of 0°, 10°, and 15°, and Reynolds numbers varying from 1.1×10^{6} to 1.7×10^{6} based on the model maximum diameter.

Test results indicate that the effect of inlet-lip bluntness is unimportant at subcritical speeds but is significant at a Mach number of 1.14 where an increase in bluntness produces an increase in the external drag. An increase in lip bluntness, however, improves the pressure recovery at all Mach numbers tested. Increasing the inward camber of the inlet lip decreases the slope of the drag curve, but lowers the pressure recovery at high mass-flow ratios and angles of attack. Outward camber greatly reduces the internal-flow distortion due to separation from the lips when the inlet is operating at angle of attack. An elliptical-lip profile is superior to a circular-lip profile from the standpoint of both external drag and pressure recovery. The transonic drag rise for a normal-shock nose-inlet configuration with a 10° half-angle conical forebody is nearly three times as great as for a similar configuration with a 5° half-angle conical forebody. Also the drag rise is initiated at a lower Mach number for the first configuration than it is for the second.

INTRODUCTION

When evaluating the performance of an air inlet, the designer must consider both the external drag and the pressure recovery of the inlet. Both of these factors are greatly influenced by the inlet-lip profile shape. Previous research (refs. 1 and 2) has shown that sharp-lipped nose inlets tend to have lower drag at supercritical Mach numbers and design mass-flow ratios than those with rounded lips. To obtain optimum thrust performance over the entire operating range from sea-level takeoff to supersonic speeds at maximum altitude, however, some degree of internal lip rounding is necessary (refs. 3 to 6).

Unfortunately, the results of previous investigations do not lend themselves well to general application because the changes in lip geometry were not sufficiently systematic. Therefore, a joint air-inlet research program was undertaken in the Langley 8-foot transonic tunnel and the Langley 4- by 4-foot supersonic pressure tunnel to determine some of the effects on inlet drag and internal-flow characteristics of a systematic variation of inlet-lip bluntness and shape. This paper presents the results obtained in the Langley 8-foot transonic tunnel.

Drag and surface-pressure measurements were made at an angle of attack of 0° with some additional drag information at $\alpha = 10^\circ$. Pressure-recovery measurements were made at 0°, 10°, and 15° angle of attack. Test Mach numbers were selected between 0.4 and 1.14. The test Reynolds number, based on the model maximum diameter, extended from approximately 1.1×10^6 to 1.7×10^6.

SYMBOLS

A cross-sectional area, sq in.

A_f fuselage maximum cross-sectional area, sq in.

a lip-profile axial dimension, in. (fig. 4)

b lip-profile radial dimension, in. (fig. 4)

C lip-profile station (fig. 4)

C_{D_e} external-drag coefficient (based on fuselage maximum cross-sectional area)

C_p static pressure coefficient, $\dfrac{p - p_0}{q_0}$

D   body maximum diameter, in.

d   diameter, in.

F   strain-gage drag force, lb

H   total pressure, lb/sq ft

$\overline{H}$ average total pressure, lb/sq ft

M   Mach number

m   internal-mass-flow rate, slugs/sec

m_1/m_0 mass-flow ratio, $\dfrac{m}{p_0 v_0 A_1} = \dfrac{A_0}{A_1}$

N   lip leading-edge station (fig. 4)

p   static pressure, lb/sq ft

q   dynamic pressure, lb/sq ft

r   radius, in.

v   velocity, ft/sec

x   distance measured parallel to axis of body, positive downstream, in. (x = 0 at leading-edge of lip IA)

x'   distance from lip leading edge parallel to axis of body, positive downstream, in.

y   lip radius, in.

α angle of attack of model center line, deg

ρ mass air density, slugs/cu ft

Subscripts:

0   free stream

1   inlet minimum area station

2   pressure-recovery-rake station

3   venturi-rake station

b   afterbody base annulus

c   strain-gage chamber

d   venturi dump

i   inner

l lip

o   outer

sonic   conditions corresponding to a local Mach number of 1.0

APPARATUS AND MODELS

Tunnel

The investigation was conducted in the Langley 8-foot transonic tunnel. The geometry and aerodynamic properties of this test section are described in references 7 and 8. A drawing of the model support system used in this investigation is presented in figure 1.

Models

The model, shown in figure 2, had a maximum diameter of 5 inches and a conical forebody section attached to a cylindrical afterbody. The inlet minimum diameter for all configurations was 2.5 inches and the duct area distribution was as shown in figure 3. In order to facilitate instrumentation, two interchangeable central bodies were employed; one of which was rigidly connected to the sting, whereas the other was linked to the sting through a flexure-type strain gage. The same afterbody assembly was used on both central bodies.

Two forebody assemblies, nose I and nose II, consisting of 5° and 10° half-angle conical forebodies, respectively, were tested. These forebodies were interchangeable on the afterbody assembly.

The inlet lips (fig. 4) were designed for a systematic variation of bluntness and shape. The profiles of lips IA to IE (ordinates given in table 1) were defined by a family of ellipses with a constant ratio of major to minor axes of 2.5 to 1. These lips incorporated a progressive change in lip bluntness, where lip bluntness is defined for this paper as the minor axis of the elliptical-lip profile expressed as a fraction of the minimum inlet radius. The values for the lips in the bluntness series are: IA, 0; IB, 0.09; IC, 0.18; ID, 0.27; and IE, 0.36. It should be noted that a variation of lip bluntness as achieved in this paper necessarily produces a variation in the forebody fineness ratio. The model configuration with the sharp lip (IA) has the highest forebody fineness ratio (2.858), and a successive increase in lip bluntness reduces the fineness ratio to a value of 1.943 for lip IE. Lips IC, IF, IG, and IH (ordinates given in table I) have the leading edge located at the same fuselage station, but vary in profile shape. Lip IC and lip IF (which has a circular profile) vary in lip leading-edge roundness, whereas lips IG, IC, and IH constitute a camber series with lip IG cambered in and IH cambered out. Lip IG was designed to improve the spillage drag characteristics of the inlet, whereas lip IH was designed to favor the internal-flow performance. Lips IIA and IIB (ordinates given in table I) were designed with different degrees of bluntness for a forebody of increased cone half-angle. The bluntness values for lips IIA and IIB are 0 and 0.18, respectively. The group I lips were interchangeable on nose I, whereas the group II lips were interchangeable on nose II.

The model was constructed of steel, and all surfaces were highly polished.

Instrumentation

The 5° half-angle conical forebody, nose I, was provided with a row of surface-pressure orifices which extended the entire length of the forebody along the center line of the upper outer surface at intervals of approximately 1.5 inches starting at station 6.915 (fig. 2). Orifices were also located on the upper outer and inner surfaces of all the inlet lips. Table II gives the spacing of these orifices on the various lips. Model base pressures were measured on the annulus at the jet exit, on the annulus at the venturi dump section, and in the gage chamber.

The pressure recovery of the flow in the duct was surveyed by six rakes of total-and static-pressure tubes located at fuselage station 10.125 (fig. 2). The mass flow and internal drag was surveyed at the venturi section by six sting-supported rakes.

The mass-flow rate through the system was varied by means of a plug, which could be moved along the sting at the jet exit to the desired location and fixed with set screws.

The afterbody assembly, which was used in the force tests, was linked to the sting through a three-component strain-gage balance.

Tests

Drag data at various mass-flow ratios were obtained for all inlets at Mach numbers of 0.6, 0.9, and 1.14 at an angle of attack of 0° and for inlets IA and IH at an angle of attack of 10°. Surface-pressure and pressure-recovery data were obtained at angles of attack of 0°, 10°, and 15° at Mach numbers of 0.4, 0.9, and 1.14 for inlets IA, IB, IC, IF, IG, and IH. Schlieren pictures of the flow field were taken for all the lips tested at an angle of attack of 0° and at Mach numbers of 0.9 and 1.14. All pressure measurements were made on a multitube manometer board.

The Reynolds number for the tests ranged from approximately 1.1×10^6 to 1.7×10^6, based on the model maximum diameter (fig. 5).

METHODS

External-Drag Coefficient

The external-drag coefficient at angle of attack of 0° is defined in this paper (see ref. 4) as:

$$C_{D_e} = \frac{F}{q_0 A_f} + \left(\frac{p_b A_b}{A_f} + \frac{p_c A_c}{A_f} + \frac{p_d A_d}{A_f} \right) -$$

$$\frac{1}{q_0 A_f} \int_{\text{venturi}} \left[\rho_3 v_3 \left(v_0 - v_3 \right) - \left(p_3 - p_0 \right) \right] dA_v \tag{1}$$

Equation (1) is the summation of the gage-pressure forces acting on the entering stream tube and the gage-pressure and viscous forces acting on the external surface. The viscous forces on the inner surface of the outer shell between the venturi and the exit stations were neglected since they were independent of the lip and nose configuration.

Appropriate corrections were applied to equation (1) when the model was at an angle of attack.

Other Variables

The pressure recovery was calculated by numerically integrating the pressure-recovery-rake data in the following manner:

$$\frac{\overline{H}_2}{H_0} = \frac{1}{A_2} \int \frac{H_2}{H_0} \, dA_2$$

The mass-flow ratio was obtained from numerical integration of the venturi-rake data.

PRECISION

The measurements and calculations of the present investigation were subject to the same type of errors which were present in reference 3. The maximum probable errors in the measurements and calculations are estimated as follows:

Free-stream Mach number . . . . ±0.003
Mass-flow ratio:
  Low mass-flow ratio (low Mach number) . . . . ±0.06
  High mass-flow ratio . . . . ±0.03
External-drag coefficient . . . . ±0.01
Integrated pressure-recovery ratio . . . . ±0.01
Pressure coefficient . . . . ±0.01

Consideration of all the factors affecting the accuracy indicates that the model angle of attack is accurate to within ±0.1°.

RESULTS AND DISCUSSION

Surface-Pressure Distributions

Surface-pressure distributions over the inlet lip and forebody configurations are shown in figures 6 and 7. In general, these figures indicate a negative pressure peak in the vicinity of the inlet lip. A second negative pressure peak exists at the maximum diameter station where the flow must accelerate through a rapid turn at the intersection of the conical forebody and the cylindrical afterbody.

The effects of variation in mass-flow ratio and lip geometry on the surface-pressure distributions at a particular Mach number are confined

to the region of the x'/D less than 1.0 behind the inlet lip. At $M = 0.9$, the data presented in figure 6 indicate that the velocities at the lip are reduced by an increase in mass-flow ratio for all lip configurations with the exception of lip IF (fig. 6(d)) for which the negative pressure peak is not adequately defined and for IH (fig. 6(f)) at $m_1/m_0 = 0.77$ where the flow appears to have separated from the external surface of the lip. At $M = 1.14$, this reduction in the velocities at the lip with increasing mass-flow ratio is apparent only for the sharp-lipped inlet (IA). The other configurations either show only small, unsystematic changes (IB and IC) or else the pressure distributions are too poorly defined to establish any definite trends (IF, IG, and IH).

The effects of lip geometry upon the surface-pressure distributions are shown in figure 7. For $M = 0.9$ and m_1/m_0 less than 1.0, the data indicate that an increase in lip bluntness from lip IB to lip IC reduces the negative pressures. For m_1/m_0 close to unity, the sharp lip (IA) exhibits no peak, whereas IB and IC show approximately the same measured negative pressures. At $M = 1.14$, an increase in bluntness from lip IB to lip IC reduces the measured velocities at the lip. Lip IA shows no negative pressure peak at maximum mass flow when the stagnation point is situated at the tip of the lip, and the flow external to the entering stream tube is not forced to accelerate through a rapid turn.

The effects of lip camber and roundness upon the surface-pressure distribution are not clearly shown as the scarcity of orifices in the critical regions precludes adequate definition of the flow phenomena at the lips.

The surface-pressure distributions at $M = 0.9$ for all lip configurations indicate that the flow over the forebody was subsonic except at the lip and maximum-diameter station. These data are supported by the schlieren pictures (figs. 8(a) and 8(b)) which establish the existence of a normal shock wave on the external surface of the lip through which the supersonic flow was decelerated to subsonic flow. These shocks generally moved rearward as the mass-flow ratio decreased. The normal shock is also displaced rearward as the bluntness is increased (IB, IC, and IE). The schlieren picture (fig. 8(a)) for lip IA at $m_1/m_0 = 0.65$ shows two normal shocks — one immediately behind the other. The first shock is believed to have been caused by the presence of an orifice in the supersonic-flow region of the lip.

Schlieren photographs of the flow about lips IA, IC, and IE at a free-stream Mach number of 1.14 are presented in figure 8(c). These pictures show that the bow wave moves closer to the inlet as the mass-flow ratio is increased. An increase in bluntness of the inlet lip at a constant value of m_1/m_0 tends to move the bow wave farther from the inlet. It is also noted that the location of the bow wave for a

blunt lip is not as sensitive to change in mass-flow ratio as for a less blunt lip. Additional schlieren pictures, not presented, show that a change in lip camber or roundness for a particular bluntness has no significant effect upon the bow-wave location.

Figure 8(c) indicates that the expansion about the lip increases in intensity as the mass-flow ratio is reduced from the choking value. This is particularly evident for the case of the sharp-lipped inlet (IA) where the shock following the expansion varies considerably in inclination to the free-stream direction as the mass-flow ratio is changed. An increase in bluntness, however, reduces the sensitivity of the expansion to changes in mass-flow ratio.

External Drag

The curves of external-drag coefficient plotted against mass-flow ratio presented in figures 9, 10, and 11 for the various lip configurations indicate that the external drag increases at a nearly linear rate as the mass-flow ratio is reduced from the maximum value. At $M = 0.9$ and m_1/m_0 approximately 0.88, there is a scatter in the data for some configurations. This apparent discrepancy is generally within the accuracy of the data and has been faired out for presentation in this report.

The effects of bluntness upon the external-drag characteristics of an inlet are shown in figure 9. At the subsonic Mach numbers of 0.6 and 0.9 there are no significant effects of lip bluntness upon the magnitude of the external drag or the slopes of the drag curves, with the exception of IE at $M = 0.9$ which is about 0.015 higher than the other configurations. At the supersonic Mach number of 1.14 an increase in lip bluntness produces an increase in external drag.

A variation of external-drag coefficient with Mach number, presented in figure 12, indicates that the transonic drag rise increases as the inlet lip becomes more blunt. As was previously pointed out in the discussion of the models, there is a fineness-ratio effect associated with blunting the lip. The plotted points on these curves were obtained from cross-plotted data but are represented by symbols for the sake of clarity.

The effects of lip camber upon the external drag of an inlet (fig. 10) are negligible at $M = 0.6$. At $M = 0.9$ and $M = 1.14$, a change from inward camber (IG) to outward camber (IH) produces an increase in the slope of the drag curve and results in greater external drag for IH than for IG at reduced mass flow. These were the expected results since, as was previously pointed out in the discussion of the models, lip IG was designed to improve the spillage drag characteristics of the inlet.

A comparison of lips IC and IF at the various test Mach numbers (fig. 10) reveals that at $M = 0.9$ and $M = 1.14$ an inlet lip with an elliptical profile has a lower external drag than an inlet lip with a circular profile. The changes in external drag with mass-flow ratio for the two lip configurations are approximately the same.

The effect of forebody fineness ratio upon the external drag is shown in figure 11. At $M = 0.6$, the drag of the two forebody configurations is approximately the same; whereas, at $M = 0.9$ and $M = 1.14$, the 10° half-angle conical forebody exhibits an external drag nearly twice that shown by nose I near the choking mass-flow ratio. Figure 12 indicates that the transonic drag rise for nose II is about three times the drag rise for nose I at $m_1/m_0 = 1.00$. It is also shown that the drag rise is initiated at a lower Mach number for the 10° half-angle conical forebody.

A comparison of the external-drag curves at 0° and 10° angle of attack for lips IA and IH is presented in figure 13. Lips IA and IH were selected inasmuch as these were thought to represent the poorest and the best of the various lip configurations, respectively, from the standpoint of both pressure recovery and internal-flow distortion. As would be expected for all Mach numbers and mass-flow ratios investigated, the external drag for both lips is greater at 10° than at 0° angle of attack. The slope of the curve for external-drag coefficient plotted against mass-flow ratio for lip IH at 10° angle of attack is about the same as at 0°, whereas the slope of the drag curve for IA is greater at 10° than at 0°. This difference is caused by the separation of the flow from the sharp lip at 10° angle of attack.

Pressure Recovery

Total-pressure-ratio distributions for lips IA, IC, IG, and IH are presented in figures 14 and 15. In general, these data show that at $\alpha = 0^O$ any effects of inlet-lip geometry upon the internal-flow characteristics of an inlet are significant only at m_1/m_0 close to 1.0. Changing the stream Mach number from 0.9 to 1.14 had no effect upon the total-pressure-ratio distributions.

A comparison of lips IA and IC, figure 14, shows that blunting the lip improves the total-pressure-ratio distribution at m_1/m_0 close to 1.0. It should be noted, however, that the superiority of IC over IA is not entirely due to bluntness alone but that an additional effect of greater length of boundary layer run for IA must be considered.

Figures 15(a) and 15(b) indicate that the internal flow separates from the lower portion of the inlet lip for all configurations tested at the maximum mass-flow ratios obtained when the inlet is at an angle of attack of 15°. A comparison of lips IA and IC at $\alpha = 15^{\circ}$ for both $M = 0.9$ and $M = 1.14$ reveals that an increase in lip bluntness helps to alleviate the separation. Also a change from inward camber (IG) to no camber (IC) decreases separation and the subsequent losses in pressure recovery. The outward cambered lip (IH), which was designed to favor the internal-flow performance of the inlet, shows the least amount of separation at $\alpha = 15^{\circ}$ of the lips for which the data for the total-pressure-ratio distribution were obtained.

Curves of pressure recovery plotted against mass-flow ratio are presented in figures 16 and 17. At $\alpha = 0^{\circ}$ (fig. 16(a)), there is no significant effect of lip geometry upon the pressure recovery at mass-flow ratios up to the choking value. However, as the angle of attack is increased, the effects of lip geometry become more important. Figures 16(b) and 16(c) show that increasing the lip bluntness (IA, IB, and IC) improves the pressure recovery of the inlet. An increase in the outward camber of the lip also aids the pressure recovery. A comparison of lips IC and IF reveals that the lip with the elliptical profile had better pressure-recovery characteristics than did the circular lip.

CONCLUSIONS

An investigation of some of the effects of inlet-lip bluntness, camber, leading-edge roundness, and forebody fineness ratio on the external-drag and pressure-recovery characteristics of a normal-shock nose inlet led to the following conclusions:

1. The effect of inlet-lip bluntness upon the external drag is unimportant at subcritical speeds but is significant at a Mach number of 1.14 where an increase in bluntness produces an increase in the external drag.

2. An increase in inlet-lip bluntness improves the pressure recovery and helps to alleviate separation of the internal flow at high mass-flow ratios and angles of attack.

3. Increasing the inward camber of the inlet lip decreases the slope of the external-drag curve and thereby lowers the external drag at reduced mass-flow ratios.

4. Increasing the inward camber of the inlet lip lowers the pressure recovery at high mass-flow ratios and angles of attack. Outward camber reduces the internal-flow distortion due to separation from the lips when the inlet plane is inclined to the free stream.

5. The elliptical-lip profile was superior to the circular-lip profile from the standpoint of both external drag and pressure recovery.

6. The transonic drag rise for a normal-shock nose-inlet config- uration with a 10° conical forebody is nearly three times as great as for a similar configuration with a 5° conical forebody. Also, the drag rise is initiated at a lower Mach number for the first configuration than it is for the second.

Langley Aeronautical Laboratory,
        National Advisory Committee for Aeronautics,
            Langley Field, Va., March 16, 1956.

REFERENCES

1. Sears, R. I., Merlet, C. F., and Putland, L. W.: Flight Determination of Drag of Normal-Shock Nose Inlets With Various Cowling Profiles at Mach Numbers From 0.9 to 1.5. NACA RM L53I25a, 1953.

2. Mossman, Emmet A., and Anderson, Warren E.: The Effect of Lip Shape on a Nose-Inlet Installation at Mach Numbers From 0 to 1.5 and a Method for Optimizing Engine-Inlet Combinations. NACA RM A54B08, 1954.

3. Pendley, Robert E., Milillo, Joseph R., and Fleming, Frank F.: An Investigation of Three NACA 1-Series Nose Inlets at Subsonic and Transonic Speeds. NACA RM L52J23, 1953.

4. Bryan, Carroll R., and Fleming, Frank F.: Some Internal-Flow Characteristics of Several Axisymmetrical NACA 1-Series Nose Air Inlets at Zero Flight Speed. NACA RM L54E19a, 1954.

5. Milillo, Joseph R.: Some Internal-Flow Characteristics at Zero Flight Speed of an Annular Supersonic Inlet and an Open-Nose Inlet With Sharp and Rounded Lips. NACA RM L54E19, 1954.

6. Blackaby, James R., and Watson, Earl C.: An Experimental Investigation at Low Speeds of the Effects of Lip Shape on the Drag and Pressure Recovery of a Nose Inlet in a Body of Revolution. NACA TN 3170, 1954.

7. Wright, Ray H., and Ritchie, Virgil S.: Characteristics of a Transonic Test Section With Various Slot Shapes in the Langley 8-Foot High-Speed Tunnel. NACA RM L51H10, 1951.

8. Ritchie, Virgil S., and Pearson, Albin O.: Calibration of the Slotted Test Section of the Langley 8-Foot Transonic Tunnel and Preliminary Experimental Investigation of Boundary-Reflected Disturbances. NACA RM L51K14, 1952.

TABLE I.- COORDINATES OF INLET LIPS

[All coordinates in inches]

Lip IB		
x	y_o	y_i
1.143	1.305	1.305
1.145	1.314	1.296
1.151	1.323	1.287
1.141	1.332	1.278
1.177	1.341	1.269
1.202	1.350	1.260
1.281	1.362	1.250
Dimensions		
Station N		1.143
Station C		1.281
a		.138
b		.055
d		1.305

Lip IC		
x	y_o	y_i
2.286	1.361	1.361
2.292	1.384	1.338
2.316	1.411	1.311
2.371	1.441	1.281
2.489	1.468	1.254
2.500	1.469	1.253
2.563	1.474	1.250
Dimensions		
Station N		2.286
Station C		2.563
a		.277
b		.111
d		1.361

Lip ID		
x	y_o	y_i
3.429	1.416	1.416
3.435	1.437	1.395
3.446	1.459	1.373
3.464	1.480	1.352
3.490	1.501	1.331
3.537	1.522	1.310
3.578	1.542	1.290
3.711	1.573	1.259
3.844	1.586	1.250
Dimensions		
Station N		3.429
Station C		3.844
a		.415
b		.166
d		1.416

Lip IE		
x	y_o	y_i
4.572	1.471	1.471
4.578	1.502	1.440
4.595	1.533	1.409
4.630	1.567	1.375
4.661	1.591	1.351
4.710	1.617	1.325
4.782	1.644	1.298
4.954	1.681	1.261
5.125	1.698	1.250
Dimensions		
Station N		4.572
Station C		5.125
a		.553
b		.221
d		1.417

TABLE I.- COORDINATES OF INLET LIPS - Concluded

[All coordinates in inches]

Lip IF		
x	y_o	y_i
2.286	1.354	1.354
2.288	1.376	1.332
2.297	1.401	1.307
2.317	1.428	1.280
2.381	1.457	1.251
2.390	1.458	1.250
Dimensions		
Station N	2.286	
Station C	2.390	
a	.104	
b	.104	
d	1.354	

Lip IG		
x	y_o	y_i
2.286	1.290	1.290
2.292	1.320	1.276
2.312	1.353	1.263
2.336	1.377	1.255
2.354	1.390	1.252
2.386	1.409	1.250
2.436	1.432	
2.652	1.481	
2.781	1.493	
Dimensions		
Station N	2.286	
d	1.290	

Lip IH		
x	y_o	y_i
2.286	1.410	1.410
2.288	1.419	1.395
2.296	1.430	1.375
2.315	1.442	1.350
2.349	1.453	1.324
2.353	1.454	1.321
2.411	1.461	1.294
2.427		1.288
2.500		1.268
2.600		1.254
2.686		1.250
Dimensions		
Station N	2.286	
d	1.410	

Lip IIB		
x	y_o	y_i
2.134	1.370	1.370
2.142	1.397	1.343
2.168	1.426	1.314
2.227	1.457	1.283
2.314	1.479	1.261
2.434		1.250
Dimensions		
Station N	2.134	
Station C	2.434	
a	.300	
b	.120	
d	1.370	

TABLE II.- ORIFICE LOCATIONS FOR INLET LIPS

[All coordinates in inches]

Lip IA		Lip IB		Lip IC	
x	y	x	y	x	y
0.250	1.272	1.281	1.250	2.563	1.250
0.696	1.311	1.177	1.269	2.371	1.281
1.143	1.350	1.151	1.287	2.316	1.311
2.515	1.470	1.143	1.305	2.292	1.338
3.829	1.585	1.151	1.323	2.286	1.361
5.086	1.695	1.177	1.341	2.292	1.384
		1.281	1.362	2.316	1.411
		2.515	1.470	2.371	1.441
		3.829	1.585	2.563	1.474
		5.086	1.695	3.829	1.585
				5.086	1.695

Lip IF		Lip IG		Lip IH	
2.390	1.250	2.386	1.250	2.686	1.250
2.317	1.280	2.336	1.255	2.427	1.288
2.297	1.307	2.286	1.290	2.353	1.321
2.288	1.332	2.292	1.320	2.315	1.350
2.286	1.354	2.312	1.353	2.296	1.375
2.288	1.376	2.354	1.390	2.288	1.395
2.297	1.401	2.436	1.432	2.286	1.410
2.317	1.428	2.652	1.481	2.349	1.453
2.390	1.458	3.781	1.493	2.411	1.461
3.829	1.585	3.829	1.585	3.829	1.585
5.086	1.695	5.086	1.695	5.086	1.695
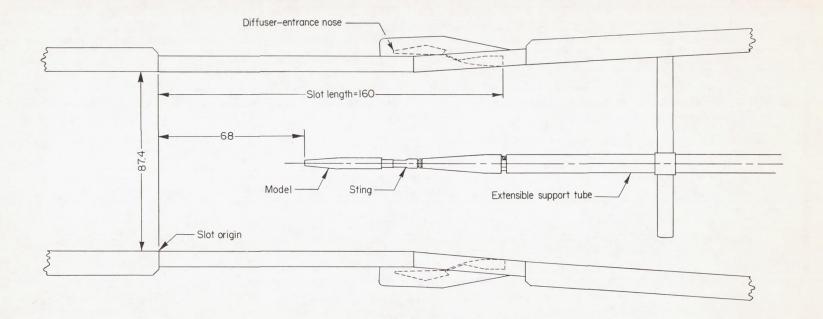
Figure 1.- Model shown mounted in Langley 8-foot transonic tunnel. All
dimensions are in inches.

Fuselage station 0

Pressure-recovery rake

5°

Maximum diameter
Fuselage station 14.287

A

B

2.500

6.125

A

19.000

B

B

9.000

18.500

Pressure model shown with nose I and lip IA

30°

6

2

5

3

4

Section A-A
Pressure-recovery rake
Fuselage station 10.125

2

6

5

3

4

2.000
5.000 D$_{max}$
3.263

Section B-B
Venturi rake
Fuselage station 27.439

Total-pressure tube

Static tube

2

6

5

3

4

Section B'-B'
Force model
Fuselage station 27.439

10°

Maximum diameter
Fuselage station 7.089

Strain-gage balance

B'

Dump-pressure tube

Exit plug
(forward position)

Base-pressure tube

2.500

3.375

Chamber-pressure tube

B'

Venturi rake

Exit plug
(rearward position)

Force model shown with nose II and lip IIA

Figure 2.- Schematic drawing of nose-inlet fuselage assemblies. All
linear dimensions are in inches.
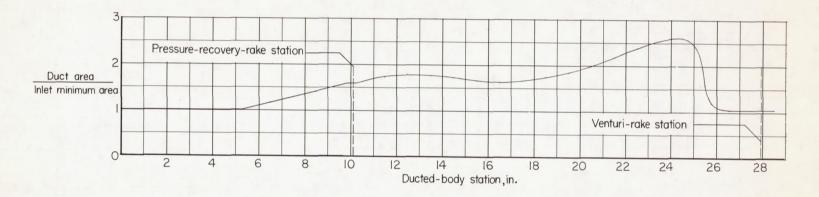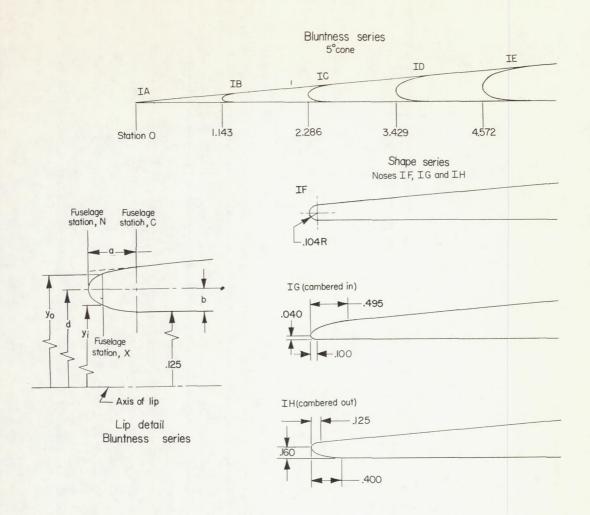
Figure 3.- Variation of inlet duct area with longitudinal station.

Bluntness series
5°cone

IA   IB   IC   ID   IE

Station 0   1.143   2.286   3.429   4.572

Shape series
Noses IF, IG and IH

IF

.104R

IG (cambered in)

.040   .495

.100

IH (cambered out)

.125

.160

.400

Fuselage   Fuselage
station, N   station, C

a

b

yo

d

yi

Fuselage
station, X

.125

Axis of lip

Lip detail
Bluntness series

IIB

IIA   .120

.300

Bluntness series
10°cone
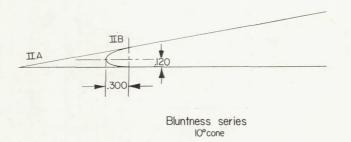
Figure 4.- Nose-inlet configurations. All dimensions are in inches.
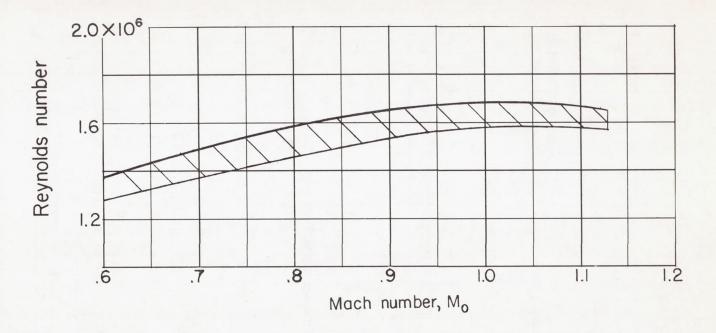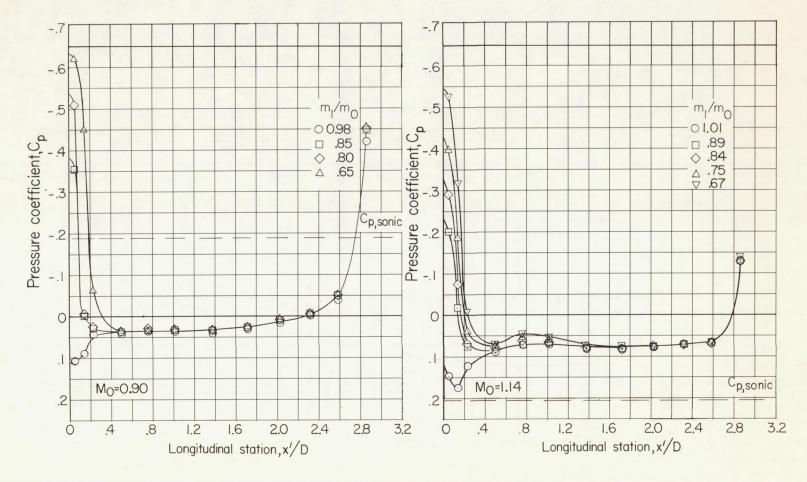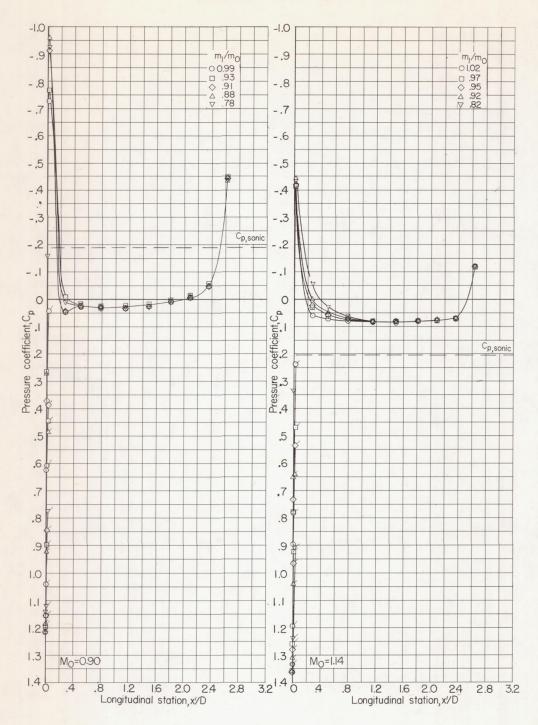
Figure 5.- Test Reynolds number range based on model maximum diameter.
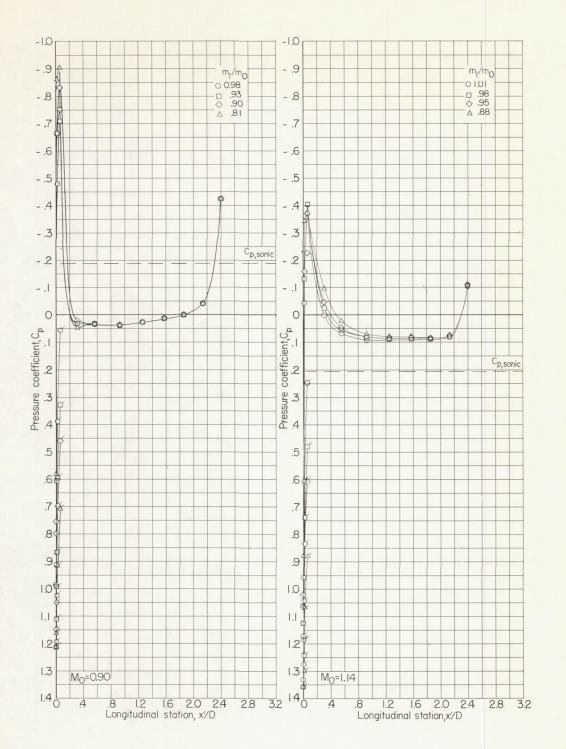
(a) Nose IA.

Figure 6.- Pressure distributions on lip and forebody. $\alpha = 0^\circ$. Flagged symbols indicate upper inner-lip pressures.
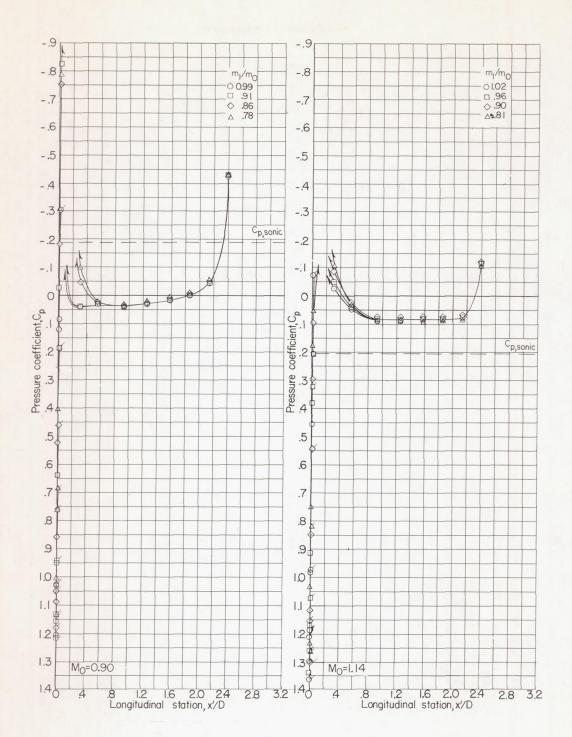
(b) Nose IB.

Figure 6.- Continued.
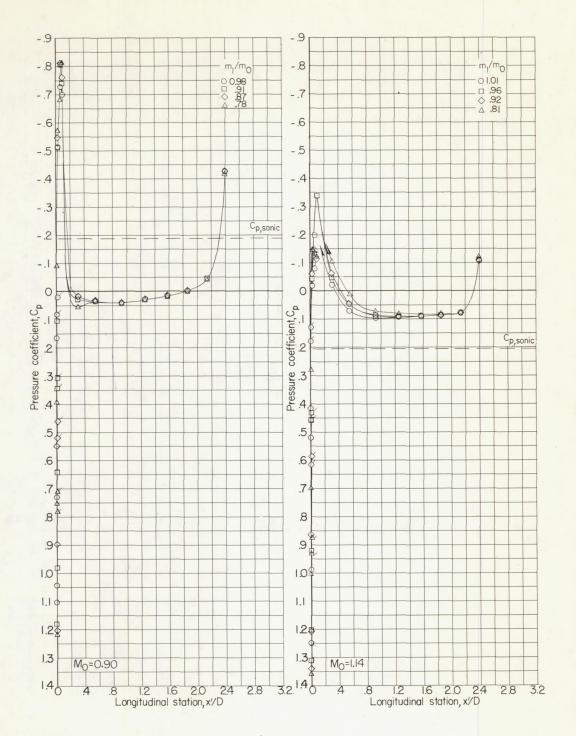
(c) Nose IC.

Figure 6.- Continued.
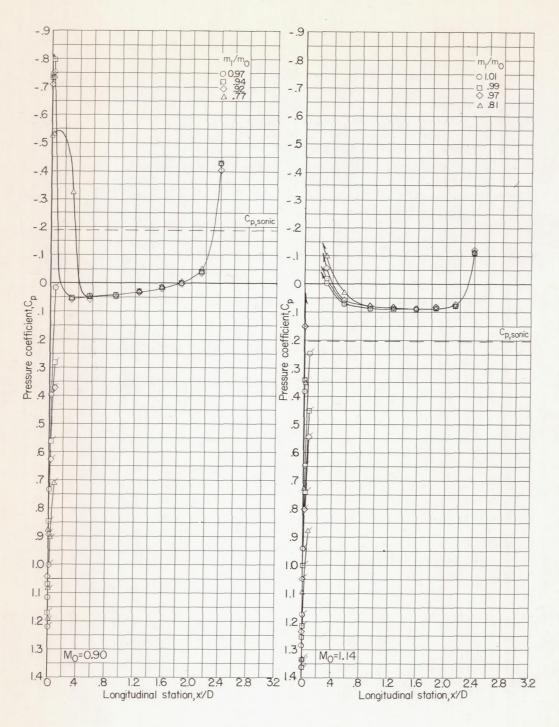
(d) Nose IF.

Figure 6.- Continued.

(e) Nose IG.

Figure 6.- Continued.

(f) Nose IH.

Figure 6.- Concluded.

(a) $M_0 = 0.90$.
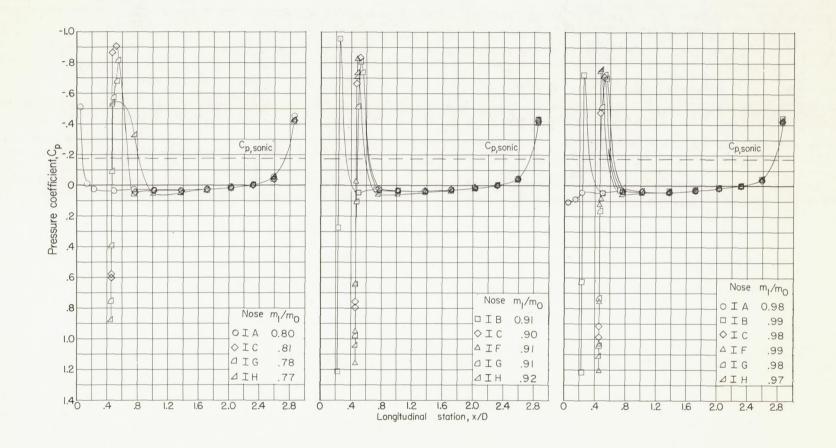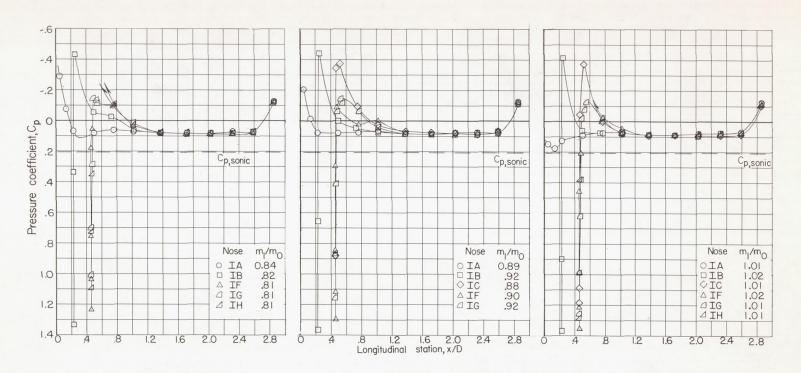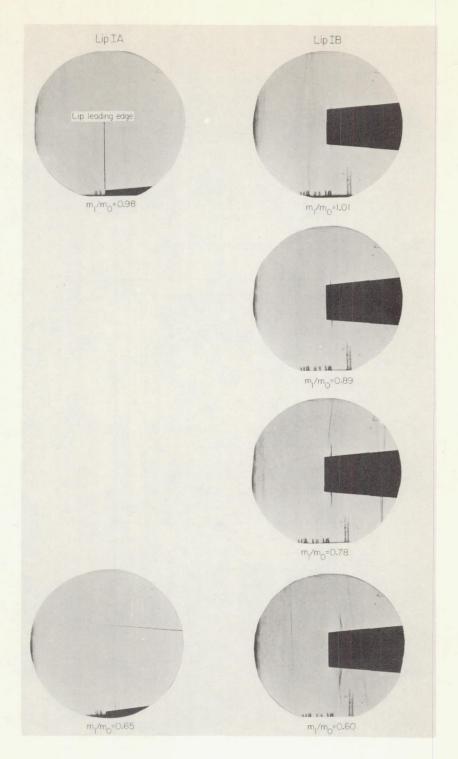
Figure 7.- Comparison of lip geometry effects upon surface pressure dis-
tribution. $\alpha = 0°$.

(b) $M_O = 1.14$.

Figure 7.- Concluded.

Lip IA

Lip IB

Lip leading edge

$m_1/m_0 = 0.98$

$m_1/m_0 = 1.01$

$m_1/m_0 = 0.89$

$m_1/m_0 = 0.78$

$m_1/m_0 = 0.65$

$m_1/m_0 = 0.60$

L-92447
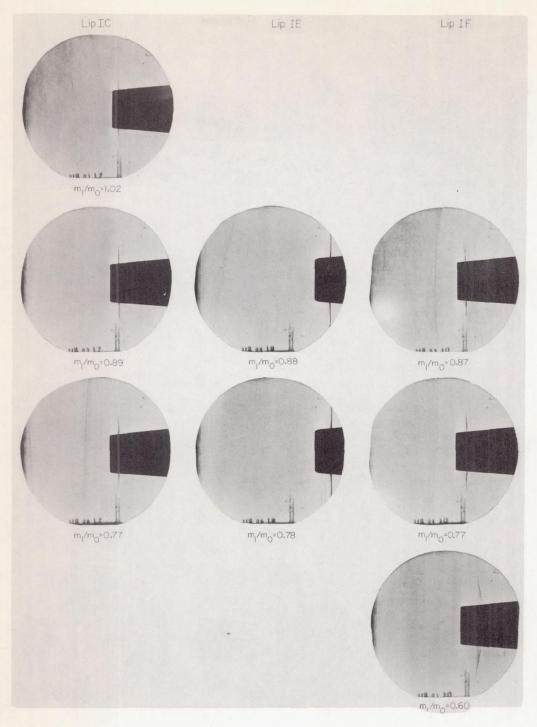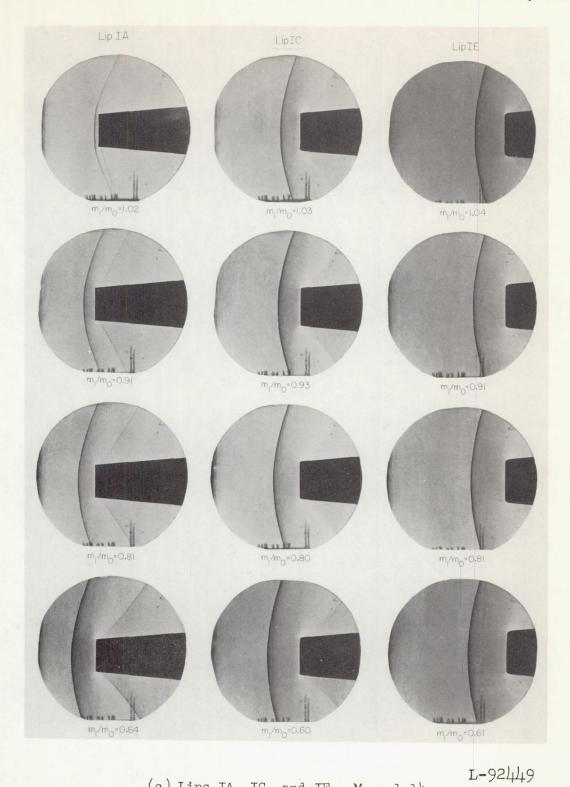
(a) Lips IA and IB, $M_0 = 0.90$.

Figure 8.- Schlieren photographs.

(b) Lips IC, IE, and IF, $M_0 = 0.90$.

L-92448

Figure 8.- Continued.

(c) Lips IA, IC, and IE, $M_O = 1.14$.

L-92449

Figure 8.- Concluded.
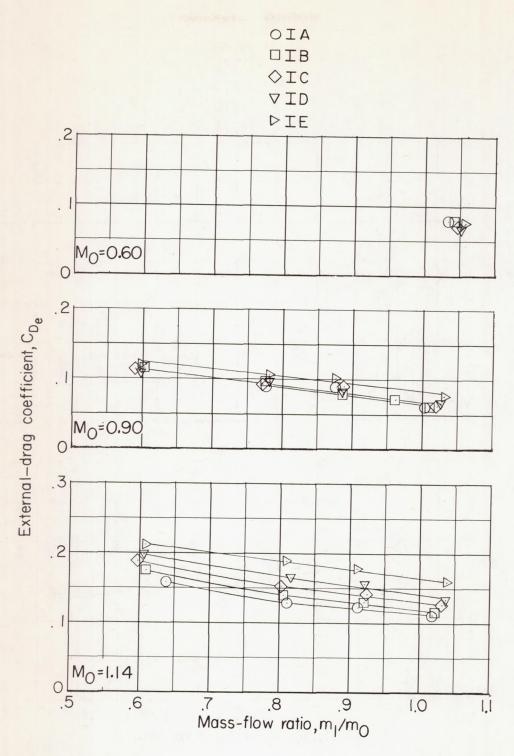
Figure 9.- Variation of external-drag coefficient with mass-flow ratio. Bluntness series; α = 0°.
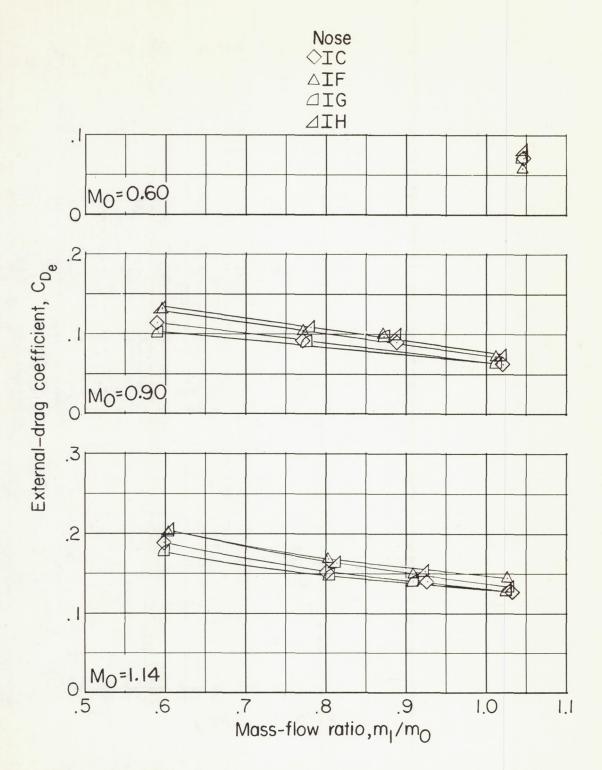
Figure 10.- Variation of external-drag coefficient with mass-flow ratio.
Shape series; $\alpha = 0^O$.
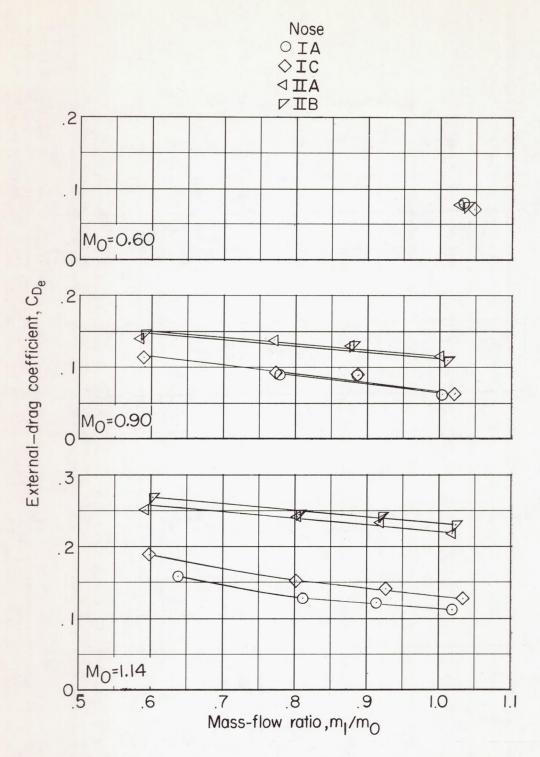
Figure 11.- Variation of external-drag coefficient with mass-flow ratio.
Effect of forebody fineness ratio; α = 0°.
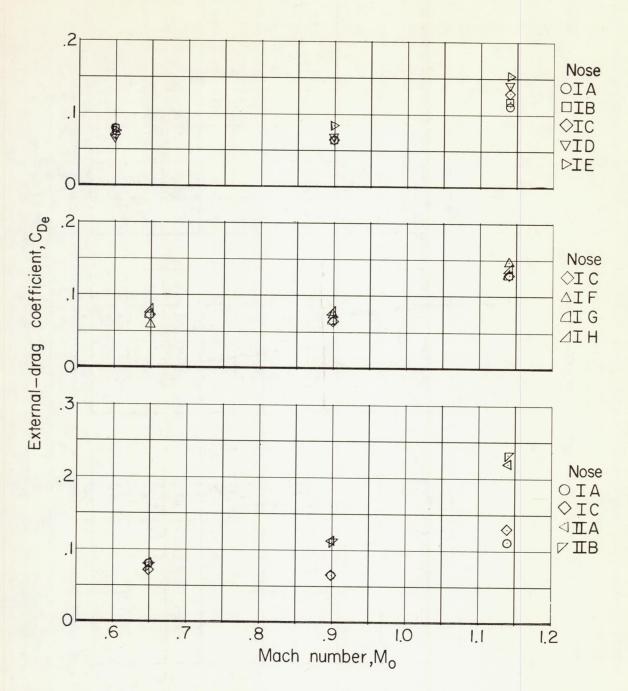
Figure 12.- Variation of external-drag coefficient with Mach number.
Mass-flow ratio, $m_1/m_0 = 1.00$; $\alpha = 0°$.
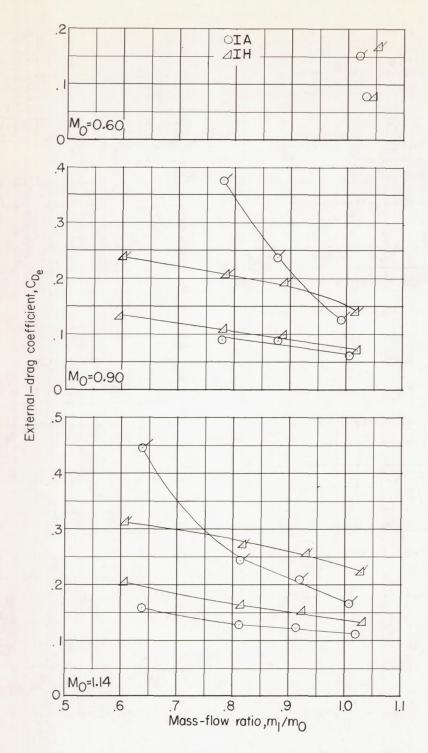
Figure 13.- Variation of external-drag coefficient with mass-flow ratio.
(Plain symbols indicate $\alpha = 0^{\circ}$; flagged symbols indicate $\alpha = 10^{\circ}$.)
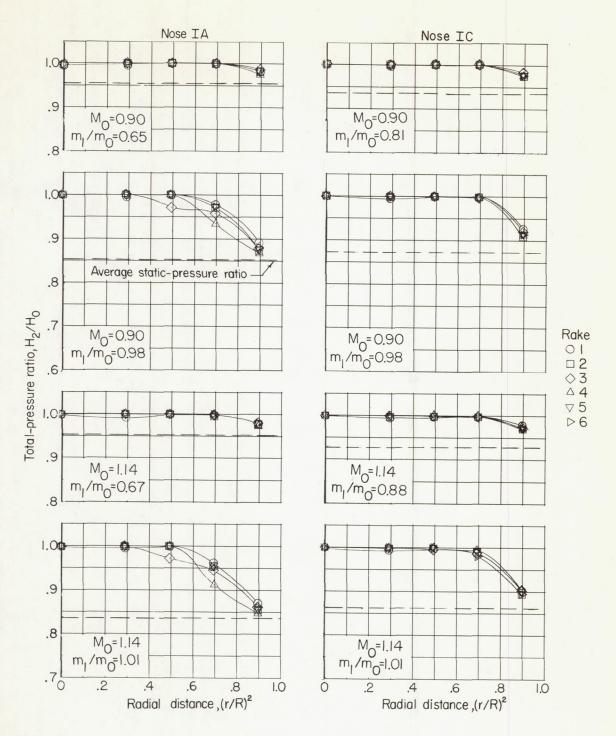
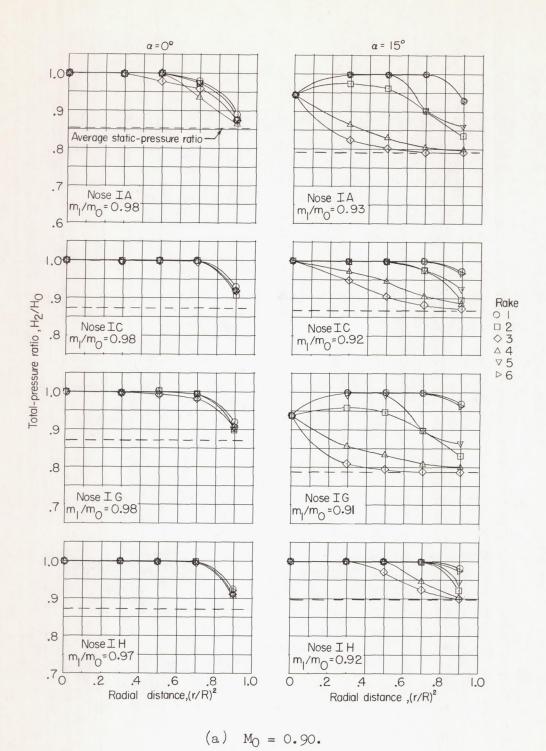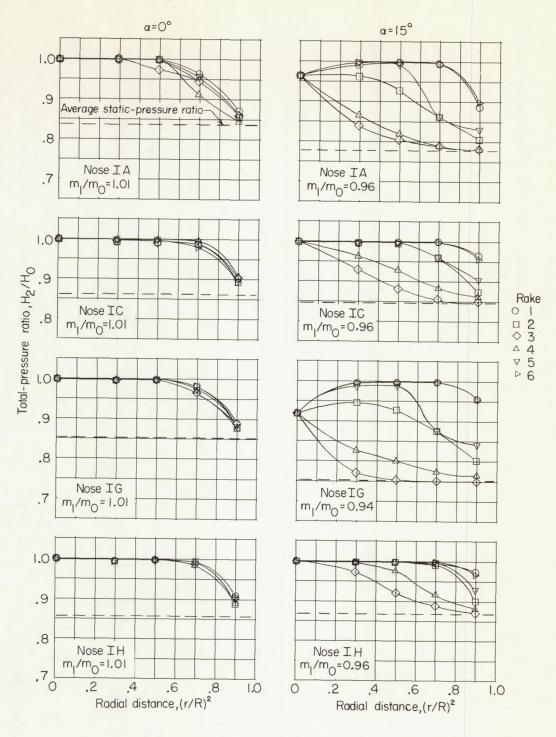Figure 14.- Radial distribution of total-pressure ratio. $\alpha = 0°$.

(a) $M_O = 0.90.$

Figure 15.- Effect of angle of attack upon radial distribution of total-
pressure ratio.

$\alpha=0°$

$\alpha=15°$

Average static-pressure ratio

Nose IA
$m_1/m_0=1.01$

Nose IA
$m_1/m_0=0.96$

Nose IC
$m_1/m_0=1.01$

Nose IC
$m_1/m_0=0.96$

Rake
○ 1
□ 2
◇ 3
△ 4
▽ 5
▷ 6

Nose IG
$m_1/m_0=1.01$

Nose IG
$m_1/m_0=0.94$

Total-pressure ratio, H_2/H_0

Nose IH
$m_1/m_0=1.01$

Nose IH
$m_1/m_0=0.96$

Radial distance, $(r/R)^2$

Radial distance, $(r/R)^2$

(b) $M_0 = 1.14$.

Figure 15.- Concluded.

(a) α = 0°.
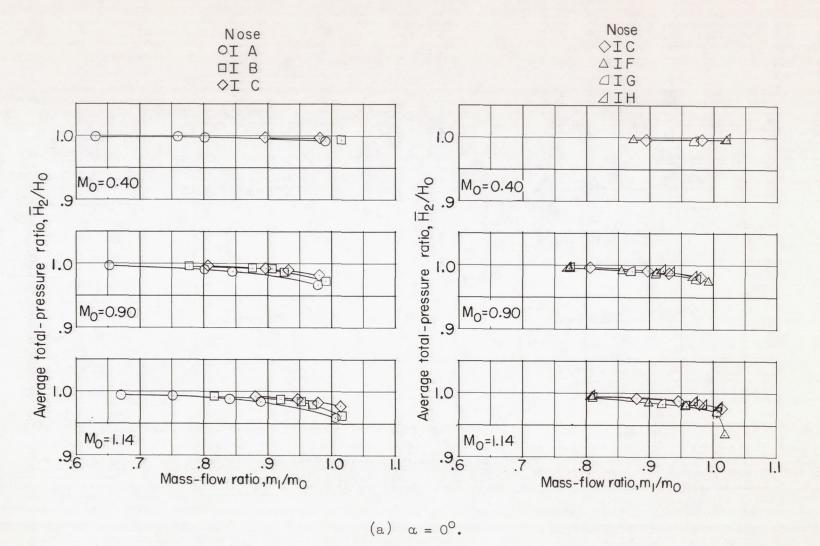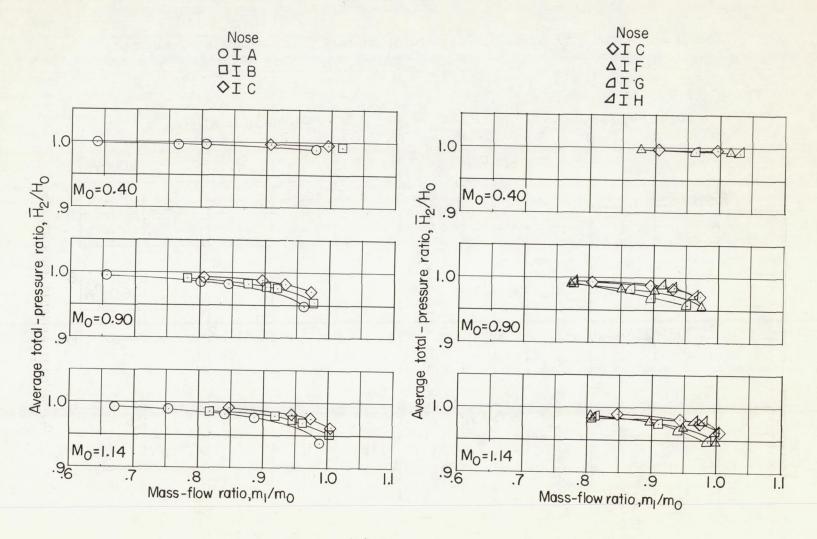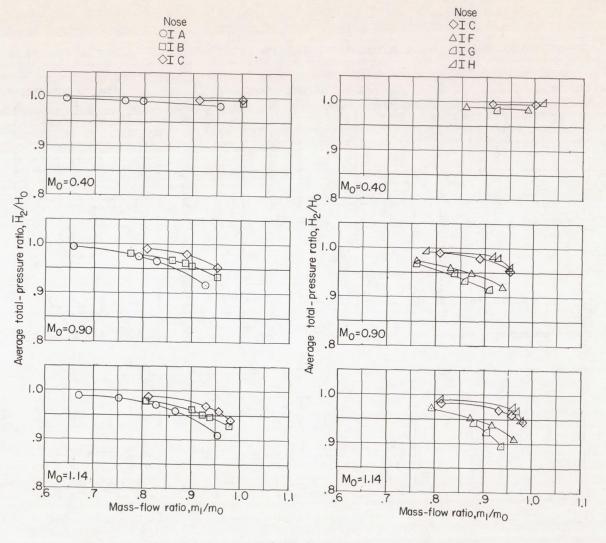
Figure 16.- Variation of average total-pressure ratio with mass-flow ratio.

Nose
○ I A
□ I B
◇ I C

Nose
◇ I C
△ I F
◁ I G
◁ I H

$M_O = 0.40$

$M_O = 0.40$

Average total-pressure ratio, $\bar{H}_2/H_0$

$M_O = 0.90$

$M_O = 0.90$

Average total-pressure ratio, $\bar{H}_2/H_0$

$M_O = 1.14$

$M_O = 1.14$

Mass-flow ratio, m_1/m_0

Mass-flow ratio, m_1/m_0

(b) $\alpha = 10^{\circ}$.

Figure 16.- Continued.

(c) α = 15°.

Figure 16.- Concluded.
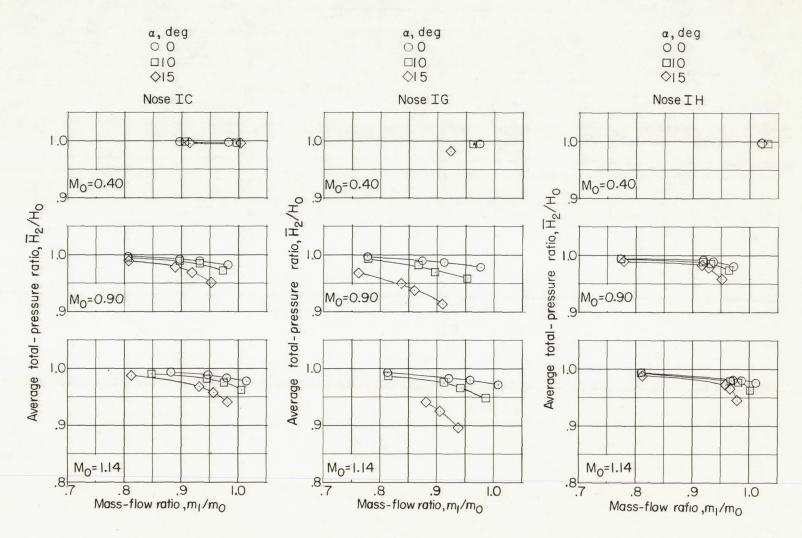
Figure 17.- Effect of angle of attack on average total-pressure ratio.